PHYSICAL REVIEW C **111**, 044313 (2025)

# Improving the predictive power of empirical shell-model Hamiltonians

J. A. Purcell,[1,2] B. A. Brown,[1,2] B. C. He,[3] S. R. Stroberg,[3] and W. B. Walters[4]
[1]*Department of Physics and Astronomy, Michigan State University, East Lansing, Michigan 48824-1321, USA*
[2]*Facility for Rare Isotope Beams, Michigan State University, East Lansing, Michigan 48824-1321, USA*
[3]*Department of Physics and Astronomy, University of Notre Dame, Notre Dame, Indiana 46556, USA*
[4]*Department of Chemistry and Biochemistry, University of Maryland, College Park, Maryland 20742, USA*

(Received 12 December 2024; accepted 26 March 2025; published 15 April 2025)

We present two developments which enhance the predictive power of empirical shell-model Hamiltonians for cases in which calibration data are sparse. A recent improvement in the *ab initio* derivation of effective Hamiltonians leads to a much better starting point for the optimization procedure. In addition, we introduce a protocol to avoid overfitting, enabling a more reliable extrapolation beyond available data. These developments will enable more robust predictions for exotic isotopes produced at rare isotope beam facilities and in astrophysical environments.

DOI: 10.1103/PhysRevC.111.044313

## I. INTRODUCTION

The nuclear shell model is a ubiquitous framework for interpreting nuclear structure data. In particular, the interacting shell model, or configuration interaction (CI) approach, quantitatively reproduces and explains a vast amount of spectroscopic data. These CI calculations require the specification of an effective Hamiltonian. While *ab initio* methods have made great progress recently in deriving these Hamiltonians from the underlying internucleon interactions, they have not yet achieved the precision obtained with phenomenological Hamiltonians adjusted to data. The gold standard for the phenomenological CI paradigm is the universal-*sd* (USD) family of Hamiltonians [1,2], which reproduce spectra with a root-mean-squared deviation of better than 200 keV. In this relatively small model space, the vast amount of available data is more than sufficient to constrain the parameters of the Hamiltonian. In contrast, many of the nuclei that will be studied in the coming decades at rare isotope facilities, including the majority of nuclei relevant for *r*-process nucleosynthesis, will live in larger model spaces where data are sparse. This increases the importance of maximizing predictive power with minimal data. In addition, the information content of various experimental data is often redundant, in terms of which parameters are constrained; in order to reliably extrapolate beyond the available data it is critical to avoid overfitting. In this paper, we (1) demonstrate that an improved *ab initio* calculation [3] provides a starting point which requires fewer phenomenological adjustments, and (2) utilize a training/testing partitioning scheme to avoid overfitting.

In Sec. II we discuss the goals and methodology of this work, including the form of our Hamiltonian constructed from *ab initio* methods, and the singular-value decomposition (SVD) method for improving the Hamiltonian by constraints to experimental data. Section III presents the mathematical methods used for the $\chi^2$ minimization and the SVD fitting algorithm. Section IV is concerned with the experimental data that were used, including a discussion justifying the inclusion and exclusion of certain observed energy levels. Our results are presented in Sec. V, and conclusions are given in Sec. VI. The Appendix presents a collection of all spectra obtained with our final Hamiltonian in comparison to experimental data.

## II. METHODS

Microscopic configuration-interaction (CI) calculations for specific regions of nuclei are based on a description in terms of a selected set of shell-model orbitals (the model space) with a Hamiltonian operator

$$H = E_0 + \sum_{\alpha} \epsilon_\alpha \hat{n}_\alpha + \sum_{\alpha\leqslant\beta,\gamma\leqslant\delta} \sum_{J} V_J(\alpha\beta;\gamma\delta)\hat{T}_J(\alpha\beta;\delta\gamma) \tag{1}$$

that is represented by the energy of the closed core $E_0$, single-particle energies (SPE) $\epsilon_\alpha$, and two-body matrix elements (TBME) $V_J(\alpha\beta;\gamma\delta)$. In principle, three-body matrix elements could be included, but they dramatically increase the complexity of the problem, and their main effect is to modify the SPE and TBME, so they are generally not treated explicitly. The SPE and TBME can be obtained from a realistic *NN* (possibly with $3N$) interaction, renormalized to the valence space in some way, for example using many-body perturbation theory [4], the shell-model coupled cluster approach [5], or the valence-space in-medium similarity renormalization group (VS-IMSRG) [6]. We use the latter approach in this work, including the effects of $3N$ interactions via the normal-ordered two-body (NO2B) approximation. This leads to values for $E_0$, $\epsilon$, and $V_J$ which are nucleus dependent [6].

A commonly applied approximation when optimizing empirical Hamiltonians is to use a nucleus-independent set of SPE and TBME. The TBME may include some smooth mass dependence, e.g., $A^{-0.3}$ [1,2,7–9]. Within this approximation the SPE and TBME can be used as parameters to achieve an improved description of measured binding energies and excitation energies (energy data) with the goal of obtaining improved wave functions and improved predictions for new energy data and for other observables.

The singular-value decomposition (SVD) method provides a systematic approach for finding the most important linear combinations of the $N_p$ SPE and TBME parameters which can be determined by the data [2,10,11]. One starts with wave functions obtained from a Hamiltonian derived from the best available *ab initio* input. With these wave functions, the expectation value of the Hamiltonian provides a linear combination of SPE and TBME for each of the $N_d$ energy data. The SVD amounts to a diagonalization of the $N_p \times N_p$ fit matrix solution to $\chi^2$ minimization, and provides singular values and associated eigenvectors (linear combinations of SPE and TBME). The largest singular values are associated with the most well-determined linear combinations, and smallest singular values are associated with the least well-determined combinations. The TBME associated with these least well-determined combinations will have some influence on the extrapolations to new energy data and to the calculations of other observables. One must choose a singular value cutoff $N_c$. Below the cutoff one can use TBME obtained from the best available *ab initio* input. This provides a new set of SPE and TBME that can be used to obtain an improved set of wave functions. One iterates the SVD fits and the wave function calculations until convergence.

Examples of Hamiltonians obtained in this way with protons and neutrons are USDA/B [1] and USDC/I [2] for the $\{0d_{5/2}, 0d_{3/2}, 1s_{1/2}\}$ ($sd$) model space, GPFX1A [7] for the $\{0f_{7/2}, 0f_{5/2}, 1p_{3/2}, 1p_{1/2}\}$ ($fp$) model space, and JUN45 [8] and jj44b (Appendix A of [9]) for the $\{0f_{5/2}, 1p_{3/2}, 1p_{1/2}, 0g_{9/2}\}$ ($jj44$) model space. For all of these Hamiltonians the root-mean-square deviation (RMSD) between the calculated and experimental energy data is 150–200 keV. This is to be compared with the results of *ab initio* type calculations over the same regions of nuclei where the RMSD is much larger (see Fig. 9 of [6] for the *sd* model space). In all of these cases, there are abundant experimental data to constrain the fitted Hamiltonian across the entire model space. However, for very exotic nuclei relevant for rare isotope beam facilities and *r*-process nucleosynthesis, the data will be sparse and strongly biased toward the most stable region of the model space. In such cases, it is possible to overfit to the available data, yielding a Hamiltonian that extrapolates poorly to more exotic nuclei.

In this paper we demonstrate that, by using an improved *ab initio* starting point and by reserving some data for validation, we can improve the predictive power of the resulting Hamiltonian when extrapolating beyond the fit data. For our application, we consider data for low-lying states for all nuclei between $^{78}$Ni and $^{100}$Sn that can be described by protons in $\{0f_{5/2}, 1p_{3/2}, 1p_{1/2}, 0g_{9/2}\}$ (the $\pi j4$ model space), which requires 4 SPE and 65 TBME with $T = 1$ associated with the valence protons. This space has been considered previously with SVD derived Hamiltonians [8,12,13], as well as those obtained using VS-IMSRG methods [14]. The data we employ consist of 22 ground-state binding energies and 167 excitation energies. The region between $^{90}$Zr and $^{100}$Sn is well established territory where many wave functions are dominated by $\{1p_{1/2}, 0g_{9/2}\}$ configurations that require only nine TBME that can be established directly from the energy data [15–21]. There are new data for nuclei close to $^{78}$Ni whose structure is dominated by the $\{0f_{5/2}, 1p_{3/2}, 1p_{1/2}\}$ subset of orbitals. Importantly, many of the single-particle energies for these orbitals associated with low-lying states in $^{79}$Cu [22] and $^{99}$In [23] are now established. The results from the IMSRG methods discussed below are also shown in Fig. 1.

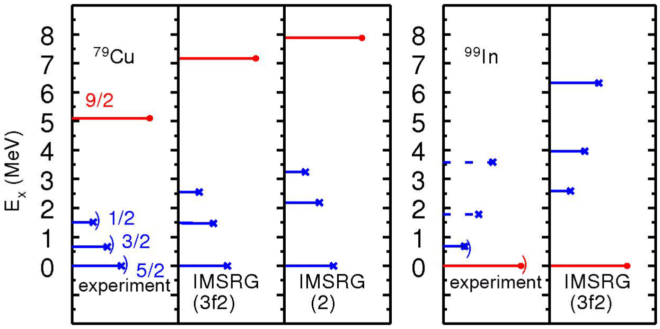

FIG. 1. Levels in $^{79}$Cu and $^{99}$In. The $J$ value is correlated with the horizontal length of the lines: blue for negative parity and red for positive parity. Experimental levels with suggested $J^\pi$ assignments are indicated by ")" [22,23]. The $9/2^+$ energy shown in the experimental panel was obtained from our p35-i3 Hamiltonian. The dashed blue lines for $^{99}$In show excitation energies based on the observations in $^{131}$In [24]. In the $\pi j4$ model space, the states for $^{79}$Cu are interpreted as single-particle states relative to a $^{78}$Ni closed shell, and states for $^{99}$In are interpreted as single-hole states relative to a $^{100}$Sn closed shell. The IMSRG results are based on calculations for $^{78}$Ni and $^{100}$Sn.

In Sec. III, we review the experimental data for nuclei between $^{78}$Ni and $^{86}$Kr. This includes a discussion of intruder states that can be attributed to orbital configurations that are not part of the $\pi j4$ model space. These intruder states are excluded from the data set used for the SVD fits.

As a starting point for our fitting procedure, we use Hamiltonians derived with the VS-IMSRG. These are obtained using the EM 1.8/2.0 $NN + 3N$ interaction [25] in a harmonic oscillator basis with frequency $\hbar\omega = 12$ MeV, truncated to 13 major shells ($2n + l \leqslant e_{\max} = 12$). We normal order with respect to the Hartree-Fock ground state of the reference and discard the residual $3N$ interaction. We then decouple the $\pi j4$ valence space, using the Magnus formulation of the IMSRG. The results labeled IMSRG(2) are obtained with the standard approximation [6], truncating all operators at the two-body level throughout the flow, including inside nested commutators. The results labeled IMSRG(3f2) include the recently introduced correction in which intermediate three-body operators arising in nested commutators are incorporated by rewriting the double commutator in a factorized form while maintaining the same computational scaling as the IMSRG(2) approximation [3]. As in Ref. [3], we include factorized terms with a one-body intermediate during the flow, and include

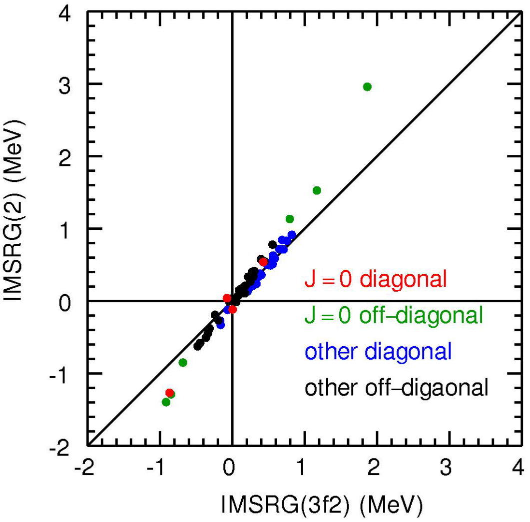

FIG. 2. Comparison of the TBME obtained with the two versions of the IMSRG method; the $y$ axis involves the two-body truncation and the $x$ axis involves the factorized approximation. The TBME are colored according to the type of overlap that they describe.

terms with a two-body intermediate at the end of the flow. We perform the procedure for two different references, $^{78}$Ni and $^{100}$Sn, corresponding to empty and full valence spaces, respectively, and take the average of the two resulting valence space Hamiltonians as our starting point for the fitting procedure.

Intuitively, the more realistic the *ab initio* Hamiltonian is, the less it needs to be modified to produce results that are in agreement with experiment. Shown in Fig. 2 is a comparison of the TBME obtained with the IMSRG(2) and IMSRG(3f2) approximations, indicating the magnitude of the uncertainty due to the many-body truncation.

These uncertainties propagate into our effective Hamiltonians, and ultimately the resulting wave functions and calculations made with them. The main difference is that the $J = 0$, $T = 1$ TBME are about 30 percent weaker for IMSRG(3f2) compared to those from IMSRG(2).

## III. MATH METHODS

### A. Initial procedure: $\chi^2$ minimization

Our starting Hamiltonian has a set of parameters $\vec{p}^s = (p_1^s, \dots, p_{N_p}^s)$. This Hamiltonian defines a starting set of eigenvectors $|\phi_k^s\rangle$ that can be used to calculate the operator overlaps $\beta_i^k$ so that each associated eigenvalue $\lambda_k$ can be calculated in Eq. (1). Then we seek to minimize the $\ell^2$-norm of the residual ($\vec{\chi}$) between the $N_d$ measured experimental energies and calculated energy eigenvalues:

$$\min_{\vec{p}\in\mathbb{R}^{N_p}} \chi^2 = \min_{\vec{p}\in\mathbb{R}^{N_p}} \sum_{k=1}^{N_d} \left( \frac{E_k^{\text{exp}} - \lambda_k(\vec{p})}{\sigma_k} \right)^2,$$

where $\sigma_k^2 = (\sigma_k^{\text{exp}})^2 + (\sigma_k^{\text{th}})^2$. We can reorganize the fitting by expanding $\lambda_k$ and defining the expected energy contribution from $H^1(\vec{p})$ to be $\epsilon_k^{\text{exp}} = E_k^{\text{exp}} - E_k^0$. Now our $\chi^2$ minimization looks like

$$\min_{\vec{p}\in\mathbb{R}^{N_p}} \chi^2 = \min_{\vec{p}\in\mathbb{R}^{N_p}} \sum_{k=1}^{N_d} \left( \frac{\epsilon_k^{\text{exp}} - \epsilon_k(\vec{p})}{\sigma_k} \right)^2.$$

We simplify the notation further first by reexpressing our data components $z_k^{\text{exp}} = \epsilon_k^{\text{exp}}/\sigma_k$ and then considering the model components:

$$z_k(\vec{p}) = \frac{\epsilon_k(\vec{p})}{\sigma_k} = \sum_{i=1}^{N_p} p_i \frac{\beta_i^k}{\sigma_k}$$

We can arrange the components of the experimental data into a data vector $\vec{z}^{\text{exp}} = [z_1^{\text{exp}}, \dots, z_{N_d}^{\text{exp}}]^T$, and similarly for the model components we can represent a model vector through matrix-vector multiplication:

$$\begin{bmatrix} z_1(\vec{p}) \\ \vdots \\ z_{N_d}(\vec{p}) \end{bmatrix} = \begin{bmatrix} \beta_1^1/\sigma_1 & \cdots & \beta_{N_p}^1/\sigma_1 \\ \vdots & \ddots & \vdots \\ \beta_1^{N_d}/\sigma_{N_d} & \cdots & \beta_{N_p}^{N_d}/\sigma_{N_d} \end{bmatrix} \begin{bmatrix} p_1 \\ \vdots \\ p_{N_p} \end{bmatrix}.$$

If we recognize that $\frac{\beta_j^k}{\sigma_k} = \frac{\partial z_k(\vec{p})}{\partial p_j}$ then the matrix above must by definition be the transposed *Jacobian* ($J^T$) of the vector-valued function $\vec{z}(\vec{p}) = [z_1(\vec{p}), \dots, z_{N_d}(\vec{p})]^T$. This allows us to reexpress our $\chi^2$ minimization as

$$\min_{\vec{p}\in\mathbb{R}^{N_p}} \chi^2 = \min_{\vec{p}\in\mathbb{R}^{N_p}} \|\vec{z}^{\text{exp}} - J^T\vec{p}\|^2$$

Minimizing this with respect to each parameter $p_j$ gives $N_p$ equations of the form

$$\begin{aligned} \frac{\partial\chi^2}{\partial p_j} &= 2\sum_{k=1}^{N_d} \left( \frac{\epsilon_k^{\text{exp}} - \epsilon_k(\vec{p})}{\sigma_k} \right) \left( -\frac{1}{\sigma_k} \frac{\partial\epsilon_k(\vec{p})}{\partial p_j} \right) \\ &= -2\sum_{k=1}^{N_d} \left( \frac{\epsilon_k^{\text{exp}}\beta_j^k}{\sigma_k^2} - \sum_{i=1}^{N_p} p_i \frac{\beta_i^k\beta_j^k}{\sigma_k^2} \right) = 0, \end{aligned}$$

which leaves us with the condition that

$$\sum_{k=1}^{N_d} \frac{\epsilon_k^{\text{exp}}\beta_j^k}{\sigma_k^2} = \sum_{k=1}^{N_d}\sum_{i=1}^{N_p} p_i \frac{\beta_i^k\beta_j^k}{\sigma_k^2}$$

Notice that if we now define the quantities

$$e_j = \sum_{k=1}^{N_d} \frac{E_{\text{exp}}^k \beta_j^k}{(\sigma^k)^2} \quad \text{and} \quad G = \begin{bmatrix} \gamma_{11} & \cdots & \gamma_{1p} \\ \vdots & \ddots & \vdots \\ \gamma_{p1} & \cdots & \gamma_{pp} \end{bmatrix},$$

where

$$\gamma_{ij} = \sum_{k=1}^{N_d} \frac{\beta_i^k\beta_j^k}{(\sigma^k)^2} = \sum_{k=1}^{N_d} \frac{\beta_j^k\beta_i^k}{(\sigma^k)^2} = \gamma_{ji} \in \mathbb{R}, \quad G = G^T,$$

we can rewrite the $N_p$ equations as a single vector equation:

$$\vec{e} - G\vec{x} = 0 \quad \longrightarrow \quad \vec{x} = G^{-1}\vec{e}. \tag{2}$$

Since the $G$ matrix is real and symmetric, it is diagonalizable. The step of solving for $\vec{x}$ shown in Eq. (2) is only possible if $G$ is invertible, meaning that none of the eigenvalues of the $G$ matrix are 0. This process can be used to find a new $\vec{x}$ that can be used to calculate new eigenvalues for the new eigenstates $|\phi_k'\rangle$, repeating until convergence. Note that $G^{-1}$ is referred to as the error matrix because its diagonal entries are the square of parameter errors and the off-diagonal entries are related to correlations between parameters.

### B. SVD proceedure

The Hamiltonian parameters are often highly correlated, and the fit can be re-expressed in terms of an orthonormal basis of uncorrelated *SVD parameters*. Since $G$ is real and symmetric, its SVD is identical to an eigendecomposition; the SVDs for $G$ and $G^{-1}$ are

$$G = ADA^T \quad \text{and} \quad G^{-1} = AD^{-1}A^T,$$

where

(1) $D \in \mathbb{R}^{p\times p}$ is a matrix of diagonal positive elements $D_{ii} > 0$,
(2) $A \in \mathbb{R}^{p\times p}$ is a rotation matrix whose columns form an orthonormal basis of our SVD parameter space,
(3) $D^{-1}$ is a diagonal matrix whose elements are inverses of the elements of $D$, i.e., $[D^{-1}]_{ii} = d_i = \frac{1}{D_{ii}}$.

With these substitutions in the result of our minimization we have

$$\vec{x} = AD^{-1}A^T\vec{e} \quad \longrightarrow \quad A^T\vec{x} = D^{-1}A^T\vec{e}.$$

Now we express the rotations of $\vec{x}$ and $\vec{e}$,

$$\vec{y} = A^T\vec{x} \quad \text{and} \quad \vec{c} = A^T\vec{e},$$

resulting in

$$\vec{y} = D^{-1}\vec{c} \quad \longrightarrow \quad y_i = d_i c_i. \tag{3}$$

Here the uncorrelated SVD parameters $y_i$ are expressed as a linear combination of the Hamiltonian parameters $x_i$ with associated errors $d_i$; explicitly,

$$\vec{y} = A^T\vec{x} = \sum_{l=1}^{p} x_l \vec{a}_l^T \quad \longrightarrow \quad y_i = \sum_{l=1}^{p} x_l [A^T]_{il}, \tag{4}$$

where $\vec{a}_l^T$ is the $l$th column of $A^T$. When $d_i$ is large the SVD parameters $y_i$ experience a large change from a correspondingly small change in the data $c_i$, meaning that the corresponding linear combination of Hamiltonian parameters $y_i$ is poorly determined by the given data set. We can establish a cutoff criterion on what is a poorly determined linear combination of Hamiltonian parameters $y_i$ based on the magnitude of the corresponding $d_i$.

### C. Fitting algorithm

(1) Starting from the best available Hamiltonian parameters $\vec{x}^s$ we construct and diagonalize the $G$ matrix to obtain $D_{ii}$ eigenvalues and the orthonormal basis for our parameter space.
(2) Mutually independent *SVD parameters* $y_i$ are determined in the fit from Eq. (4). Explicitly,

$$y_i = d_i c_i = d_i \sum_{l=1}^{p} e_l [A^T]_{il}.$$

Simultaneously, linear combinations of *ab initio Hamiltonian parameters* are determined from Eq. (4). Explicitly,

$$\vec{y}^* = A^T\vec{x}^* \quad \longrightarrow \quad y_i^* = \sum_{l=1}^{p} x_l^* [A^T]_{il}.$$

(3) One defines a cutoff criterion $\delta$, and updated linear combinations $\vec{y}^a$ are defined by only adopting well-determined values $y_i$ with respect to this cutoff, and leaving *ab initio* values $y_i^*$ for the rest:

$$y_i^a = \begin{cases} y_i & (d_i \leqslant \delta), \\ y_i^* & (d_i > \delta). \end{cases}$$

The number of well-determined linear combinations is $N_d$.
(4) With the updated set of model parameters $\vec{y}^a$ one recovers the Hamiltonian parameters by inverting the rotation:

$$\vec{x}^a = (A^T)^{-1}\vec{y}^a.$$

(5) This set of Hamiltonian parameters takes the place of $\vec{x}^s$ as input to the first step of this algorithm, and is used to obtain the next set of parameters $\vec{x}^b$. This process is repeated until convergence.

## IV. EXPERIMENTAL DATA FOR $N = 50$ ISOTONES

For the data used as input for the SVD fits we chose levels which have reliable excitation energies and $J^\pi$ values as determined by various types of experiments. In addition, there are levels not included in the SVD fits: those with uncertain $J^\pi$ values and those that can be considered as intruder states into the $\pi j4$ model space. We use experimental data from the Evaluated Nuclear Structure Data Files (ENSDF) [26]. The purpose of this section is to review the relatively new data for the nuclei $^{78}$Ni up to $^{86}$Kr with regard to these criteria for inclusion. The subsequently chosen data are given in [27].

The structure of $^{78}$Ni has been studied via knock-out reactions and shows a group of excited states between 2.6 and 4.0 MeV [28]. Levels with spins and parities of $2^+$ and $4^+$ are suggested at 2.60 and 3.18 MeV, respectively. The relatively high excitation of these states indicates that the wave function of $^{78}$Ni is dominated by closed-shell configuration of $Z = 28$ for protons and $N = 50$ for neutrons. For protons, a $0f_{7/2}$ proton can be moved across the $Z = 28$ proton gap into the $0f_{5/2}$ and $1p_{3/2}$ orbitals, leading to a multiplet of states with $J^\pi$ ranging from $1^+$ to $6^+$. For neutrons, a $0g_{9/2}$ neutron can be moved across the $N = 50$ shell gap into the $0d_{5/2}$ orbital, leading to a multiplet of states from $2^+$ to $7^+$. Also for neutrons, a $1p_{1/2}$ neutron can be moved across $N = 50$ into the $0d_{5/2}$ orbital, leading to states with $2^-$ and $3^-$.

The level structure of $^{79}$Cu has also been studied in knock-out reactions [22]. Two low-lying levels are proposed at 0.656 and 1.511 MeV with the gamma-decay sequence of 1.511 to 0.656 MeV to the ground state. These experimental energies are compared to shell-model predictions in Fig. 1. All of these predictions give an ordering of $1/2^-$, $3/2^-$, and $5/2^-$

corresponding to single-particle configurations of $1p_{1/2}$, $1p_{3/2}$, and $0f_{5/2}$, respectively.

The $^{79}$Cu ground-state spin-parity is not measured. The lighter Cu isotopes are measured to have $^{71}$Cu ($J = 3/2$), $^{73}$Cu ($J = 3/2$), $^{75}$Cu ($J = 5/2$), and $^{77}$Cu ($J = 5/2$) [26]. Shell-model calculations give negative-parity ground states. The energy differences between the lowest levels with $J = 3/2^-$ and $J = 5/2^-$ obtained with the JUN45 Hamiltonian [8] in the $jj44$ model space are shown in Fig. 6. They are compared with experiment for $^{69,71,73,75}$Cu using the energies of the states that are suggested to have $J = 3/2$ and 5/2 [26]. For $^{79}$Cu we give the experimental results assumming a ground state and first excited states with $J^\pi$ of $5/2^-$ and $3/2^-$ respectively (solid black line) and $3/2^-$ and $5/2^-$ respectively (dashed black line). The systematics of these energy differences compared to theory are consistent with the ground state of $^{79}$Cu having $J^\pi = 5/2^-$, with the first excited state at 0.656 MeV having $J^\pi = 3/2^-$. When compared to the shell-model calculations in Fig. 1, the second-excited state at 1.511 MeV is expected to have $J^\pi = 1/2^-$. The sequence of gamma decays observed in [22] is consistent with the $(1/2^-, 3/2^-, 5/2^-)$ sequence. In the single-particle model this gives a $1p_{1/2} - 1p_{3/2}$ spin-orbit splitting of 0.855 MeV. This smaller the value of 1.66 MeV shown by the MCSM calculations in Fig. 2 of [22]. The experimental $1/2^-$-$3/2^-$ splitting in in $^{131}$In is suggested to be 988 keV [29].

Other excited states in $^{79}$Cu are observed starting at 2.9 MeV. It is natural to understand these as intruders coming from the knockout of an $0f_{7/2}$ proton in $^{80}$Zn leading to 2p-1h states in $^{79}$Cu. Three transitions at 2.94, 3.88, and 4.30 MeV of about equal intensity that decay directly to the ground state and could represent fragments of the $0f_{7/2}$ hole strength.

The first excited $2^+$ level in $^{80}$Zn was identified in a Coulomb excitation study at 1.492 MeV [30]. The Coulex experiment obtained $B(E2, \uparrow) = 20.1(16)e^2\mathrm{fm}^4$. Further level structure has been provided from knock-out reactions, where a $4_1^+$ level is placed at 1.93 MeV [31]. In [31] three other levels are identified at 2.627, 2.820 and 3.174 MeV. The latter two decay only to the $4_1^+$ level. The experimental energies are compared to those from the JUN45 [8] and MCSM [32] Hamiltonians in Fig. 4 of [31]. With only two protons in the $0f_{5/2}$ and $1p_{3/2}$ orbitals beyond $^{78}$Ni, the maximum positive-parity spin is $4^+$. Lifetimes and $B(E2)$ values have been determined for both the $2^+$ and $4^+$ levels [33].

Level structure for $^{81}$Ga comes from extensive study of the beta decay of the $5/2^+$ ground state of $^{81}$Zn, as well as by both multinucleon transfer (MNT) and knock-out reactions. A recent decay scheme was obtained using laser-ionized $^{81}$Zn and has provided the most detail [34]. The ground-state $5/2^-$ assignment is supported by laser hyperfine methods [35]. Two excited $3/2^-$ levels are identified, along with one clear $9/2^-$ level and one clear $11/2^-$ level [36]. $11/2^-$ is the highest spin that can be obtained by three protons in the $0f_{5/2}$ and $1p_{3/2}$ orbitals. Levels proposed at higher spins would have to involve either the $0g_{9/2}$ proton orbital or intruder states coming from the neutron excitations across the $N = 50$ shell gap. A possible higher-spin level has been reported by both [36,37] at 2.766 MeV that decays to the $11/2^-$ level. Refrence [36] also reports on the gamma decay from a level at 3.093 to the 2.766 MeV level, that could have even higher spin. Transitions at 770 and 990 keV were observed in ($p$,2$p$) reactions that feed into the $11/2^-$ level at 1.952 MeV [38].

The basic level structure for $^{82}$Ge was provided by beta decay of the $2^-$ ground state of $^{82}$Ga [39,40] and beta-delayed neutron decay of the $5/2^-$ ground-state of $^{83}$Ga, and also by Coulomb excitation, MNT studies [41–44], and fission-product gamma-ray studies [45]. Triple coincidences between gamma rays (in MeV) at 1.348 ($2^+$), 0.938 ($4^+$), and 0.940 ($6^+$) establish the yrast sequence. As $6^+$ is the highest possible spin for four protons in the $0f_{5/2}$ and $1p_{3/2}$ levels, this level would have to arise from some cross-shell excitation, or involvement of the $0g_{9/2}$ proton orbital. A proposed $7^+$ level at 3.948 MeV has been reported [46] that decays to the $6^+$ level at 3.228 MeV. These $5^+$, $6^+$, $7^+$ states are understood as coming from the excitation of a neutron in the $0g_{9/2}$ orbital into the $1d_{5/2}$ orbital across the $N = 50$ shell gap [46,47]. These high-spin particle-hole configurations are also observed in $^{84}$Se, $^{86}$Kr, and $^{88}$Sr [46] at increasingly higher excitation energy.

The $2_2^+$ MeV level is placed at 2.216 MeV by strong population in all of the decay studies as well as the presence of a 2.216 MeV ground-state transition. The $0_2^+$ level at 2.333 MeV is similarly observed in decay studies with no ground-state transition. Two levels at 2.702 and 2.714 MeV observed in all of the decay studies, but not observed in the MNT and fission-gamma studies, are possible $3^+$ and $1^+$ levels, respectively. Two levels at 2.883 and 2.933 MeV are observed in decay, MNT, and fission studies that decay only to the two lower-energy $4_1^+$ and $4_2^+$ levels and are candidates for $4^+$ and $5^+$ assignments. The $B(E2)$ value for the 1.348 MeV level has been measured by [48].

The level structure of $^{83}$As with 33 protons has the most complex structure among the odd-proton $N = 50$ isotones. It has five valence protons and is exactly half way from $Z = 28$ to $Z = 38$. The maximum spin available by breaking both pairs of protons that occupy the $0f_{5/2}$ and $1p_{3/2}$ orbitals would be $13/2^-$. Extensive data exist for the structure of $^{83}$As from decay and MNT reaction studies. With five protons, the Fermi level has moved up in energy to the point that a $9/2^+$ state associated with the $0g_{9/2}$ proton state should be observed. However, firm identification has remained elusive. A candidate is present at 2.777 MeV that has been assigned $(9/2^+)$. [49]. However, in other studies, no level was assigned as $9/2^+$ [50–52]. The gamma decay data clearly show low-energy levels that have should have proton configurations, then a gap around 3 MeV where the neutron particle-hole states should be present [53]. As in $^{81}$Ga, three excited levels in $^{83}$As at 0.307, 1.544, and 1.867 MeV are clearly identified as $3/2^-$, $9/2^-$, and $11/2^-$, respectively.

Extensive data are also present for the structure of $^{84}$Se. Not only from beta decay and multinucleon transfer (MNT) studies, but also from the $^{82}$Se$(t, p)^{84}$Se two-neutron transfer reaction [54], and where cross-shell neutron states are possible, the level density rises rapidly. Neutron excitations across the shell gap give rise to intruder states, and one expects similar intruder states in even-even nuclei across the region of interest. Levels populated in beta decay were reported by Hoff *et al.* [55]. High-spin structures have been reported by several groups [43,51].

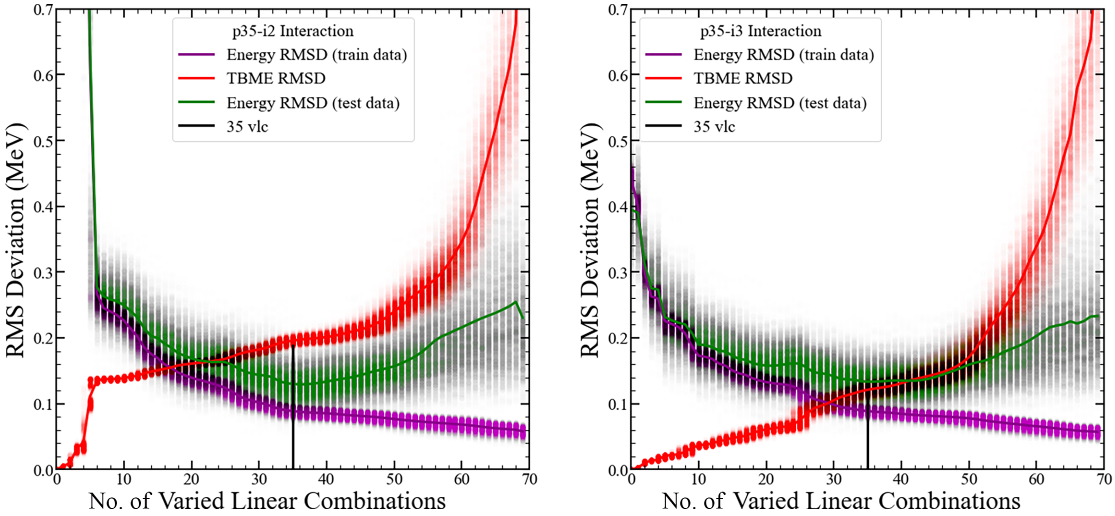

FIG. 3. Results of the SVD fits as a function of the number of varied linear combinations (VLC) of parameters. The left-hand side shows results used to obtain the p35-i2 Hamiltonian, and the right-hand side shows results used to obtain the p35-i3 Hamiltonian. The purple points show the energy RMSD between theory and experiment as a function of the number of VLC, and the red points show the TBME RMSD between the IMSRG and fitted Hamiltonians. The lines are the results for the pn-i2 and pn-i3 Hamiltonians. We also show points for the 2000 batches of randomly sampled experimental training data discussed in the text: purple points for the training energy data set and green points for the predicted data set.

Three prominent higher-spin levels have been observed at 3.372 [$6^+$], 3.639 [$5^+$], and 3.704 [$6^+$] MeV with the spin and parity assignments derived from respective Coulex data [54,56,57]. A proposed $7^+$ level has been identified in several papers at 4.407 MeV. Unlike $^{82}$Ge, it is possible to obtain spin and parity of $7^+$ by aligning all six protons in the $0f_{5/2}$, $1p_{3/2}$, and $1p_{1/2}$ orbitals [46]. Two $0^+$ levels below 3 MeV are identified in both reports at 2.247 and 2.655 keV. Gamma-ray transitions from both of these levels are seen by cross-correlations in the Carpenter data set [43]. Three other 0+ levels are proposed at 1.967, 2.716, and 2.740 MeV for which no gamma transitions are observed.

The level structure of $^{85}$Br is quite important for these studies as the data for the spins and parities are on a far firmer basis. Polarized proton pickup in the $^{86}\mathrm{Kr}(d,{}^3\mathrm{He})\,{}^{85}\mathrm{Br}$ reaction provides definitive data for the locations of the $3/2^-$, $5/2^-$, and $1/2^-$ states at 0, 0.345, and 1.191 MeV, respectively. These are associated with $1p_{3/2}$, $0f_{5/2}$, and $1p_{1/2}$ single proton hole states. Angular distribution data for the high-spin levels also provide a definite location of the $9/2^+$ level at 1.859 MeV that is associated with proton excitation into the $0g_{9/2}$ orbital. The yrast $9/2^-$ and $11/2^-$ levels observed in the lower-$Z$ isotones are clearly identified at 1.572 and 2.165 MeV, respectively.

Excellent data are available for the levels of $^{86}$Kr. The new beta-decay data from the $1^-$ $^{86}$Br ground state leads directly to a certain $2^-$ assignment for the level at 4.316 MeV [58]. There is also good agreement for the high-spin levels from studies by two different groups [59,60]. There are Coulex data for the $2^+$ and $3^-$ levels and a surprising long 3-ns half-life for the $4_1^+$ level.

The data chosen for the SVD fit are given in [27]. The majority of these data have experimental uncertainties of a few keV. The exceptions are: 100 keV for the $^{79}$Cu ground state [61], 77 keV for the $^{99}$In ground state [62], 37 keV for the $^{99}$In first excited ($1/2^-$) state [23], and 240 keV for the $^{100}$Sn ground state [61,63]. In order to constrain the SPE at the beginning and the end of the $\pi j4$ model space, smaller uncertainties of 50 keV (without the theoretical error of 150 keV) were used for the $3/2^-$ and $1/2^-$ excited states observed for $^{79}$Cu and for the $3/2^-$ and $5/2^-$ excited states extrapolated for $^{99}$In.

## V. RESULTS

The theoretical uncertainty $\sigma_{\mathrm{th}}$ is taken to be 150 keV. Most experimental uncertainties are on the order of a few keV, with a larger uncertainties of a few hundred keV in the some binding energies. The value of the $\sigma_{\mathrm{th}}$ is chosen to give a $\chi^2$ of about unity for the final fit. This effectively makes the weights of all energy data about equal. Changing $\sigma_{\mathrm{th}}$ in the range of 100–200 keV has very minimal effect on the results.

Figure 3 shows the RMSD for the two different IMSRG starting points as a function of the number of varied linear combinations (VLC) of parameters. The resulting Hamiltonians will be labeled by p$n$-i$a$ where $n$ indicates the number of VLC, and $a$ indicates the *ab initio* starting Hamiltonian, $a = 2$ for IMSRG(2) and $a = 3$ for IMSRG(3f2). The purple line shows the energy-RMSD between the calculated and experimental energy data.

Both starting points approach a similar level of energy RMSD as the number of VLC increases. The major difference between the approach to this threshold is shown by the red points, which shows the RMSD between the fitted and *ab initio* TBME. For IMSRG(2) the TBME RMSD goes above the 200 keV level with six VLC, while for the results for IMSRG(3f2) do not reach this level until around 55 VLC. It can also be seen that the energy RMSD for the fitted data set

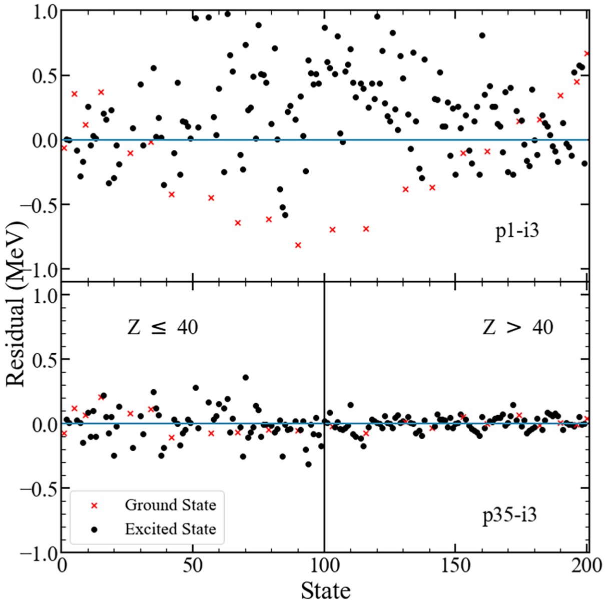

FIG. 4. Residual between states calculated from effective Hamiltonian with both 1 VLC (p1-i3) and 35 VLC (p35-i3), and corresponding experimental states used to generate the effective Hamiltonian. Both effective Hamiltonians are obtained from the IM-SRG(3f2) starting point. We note that the p35-i3 energy differences are larger for $Z \leqslant 40$ (120 keV) compared those above that (50 keV). The main reason is that the higher-mass data is dominated by only nine TBME associated with the $\{1p_{1/2}, 0g_{9/2}\}$ orbitals, whereas the lower mass data is dominated by 30 TBME associated with the $\{0f_{5/2}, 1p_{3/2}, 1p_{1/2}\}$ orbitals.

falls substantially after only one VLC for IMSRG(3f2), while IMSRG(2) requires nearly 15 VLC to reach the same level of accuracy. These results highlight the improvement made for the TBME by the IMSRG(3f2) method. The deviations for each state in the fitted energy data obtained with the p1-i3 and p35-i3 Hamiltonians are shown in Fig. 4. The IMSRG(3f2) Hamiltonian should provide better input for the undetermined SVD linear combinations compared to IMSRG(2). The SPE and TBME for the p35-i3 Hamiltonian and the numerical results of the p35-i3 SVD fit in comparison to experimental data are given [27].

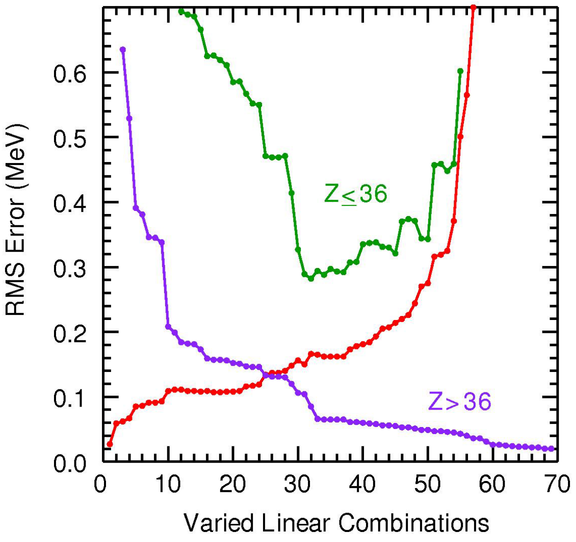

FIG. 5. Results obtained when the fitted data set is restricted to $A > 86$. See caption of Fig. 3.

An essential purpose of these effective Hamiltonians is to achieve some level of predictive power; this is highlighted in Fig. 3. To obtain the scatter of the points around the central fit values as well as the green points in this figure, all of the known experimental data for this model space were randomly partitioned into training (80%) and testing (20%) batches. The training batch was used to vary the parameters of our Hamiltonian, and the testing set was used in the calculation of RMSD; in this way our fitted Hamiltonian is predicting the results of data that it had not seen in the fitting procedure. The sampling process was repeated 2000 times to generate a distribution of calculations for each VLC, and for each set of Hamiltonian parameters. The green curve highlights the predictive capacity of each Hamiltonian as the number of VLCs is increased. It can be seen that each Hamiltonian approaches an energy RMSD minimum (a maximum for the predictive power) at about 35 VLC. In fact the RMSD is reasonably small over the range of 15–35 VLC. This is significant because it indicates that we can achieve some benchmark level of predictive power with fewer modifications to our starting Hamiltonian with the factorization method given by [3]. This becomes critically significant when one considers effective Hamiltonians for larger model spaces where producing these effective Hamiltonians and using them to make predictions becomes computationally intensive, or where data are sparse or redundant in terms of constrained parameters.

The calculations presented in Fig. 5 sampled from the full range of data $28 \leqslant Z \leqslant 50$, so the predictions are in some sense an interpolation. It is of great interest to also understand the robustness of extrapolations beyond the fit data. To do this, we partition the data so that the training data only contain $Z > 36$, and consider the RMSD for $Z \leqslant 36$. We find that the RMSD in the neutron-rich validation set decreases as the number of VLC is increased, up to 35, where we obtain an RMSD of approximately 300 keV. Beyond 35 VLC, the RMSD grows again, indicating that we have begun to overfit, and extrapolative power deteriorates.

We found that two markedly different starting Hamiltonians can be tuned to produce quite similar results when a robust dataset and fitting method are implemented. The degree to which these starting Hamiltonians must be modified intuitively depends on how successful the initial parameters are at reproducing the known experimental data. The goal is to produce wavefunctions that are realistic and predictive. The spectra predicted from our p35-i3 Hamiltonian are compared with their experimental counterparts, and in comparison to all experimental data are shown in the Appendix.

## VI. CONCLUSIONS

We find that the factorized approximation of IMSRG(3f2) given by [3] produces a starting Hamiltonian that requires less modification to reproduce experimental data than *ab initio*

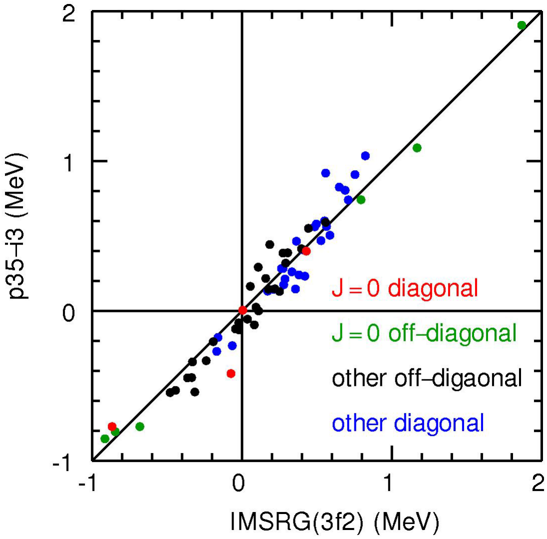

FIG. 6. Comparison of the IMSRG(3f2) and p35-i3 TBME.

Hamiltonians produced by other methods, meaning that this Hamiltonian is inherently more realistic; a result illustrated clearly in Figs. 3 and 6. The TBME RMSD is much smaller with the recently introduced VS-IMSRG(3f2) corrections involving three-body operators. Thus, 3f2 should provide a better input for the linear combinations of parameters that cannot be determined from VLC fits to energy data. In addition, we have demonstrated that utilizing the RMSD from the training/validation partitioning in the fit procedure helps protect against overfitting, and yields more robust extrapolation to data beyond those used in the fit. The resulting Hamiltonian predicts a subset of the experimental spectra for all nuclei in the $\pi j4$ space to within a 100–130 keV RMSD.

The figures in the Appendix show the calculated spectra for all nuclei in comparison to experimnental data. Many of the predicted theoretical states are not yet observed in experiment. We predict the binding energy of $^{100}$Sn [27], a doubly magic nucleus that is of imminent experimental interest because it is so proton rich, and lies at the edges of stability. Also one needs to confirm our extrapolations for the excited states of $^{99}$In by their gamma dcay following one-proton knockout reactions on $^{100}$Sn. In the other extreme in $^{79}$Cu, one needs to confirm our extrapolated excitation energy for the $9/2^+$ excited state.

## ACKNOWLEDGMENT

We acknowledge support from NSF Grants No. PHY-2110365 and No. PHY-2340834.

## DATA AVAILABILITY

The data supporting this study's findings are available within the article.

## APPENDIX: COMPARISON OF EXPERIMENTAL AND THEORETICAL ENERGY LEVELS

Figures 7–27 compare theory and experiment for all nuclei in the $\pi j4$ model space. The color of each line gives the parity

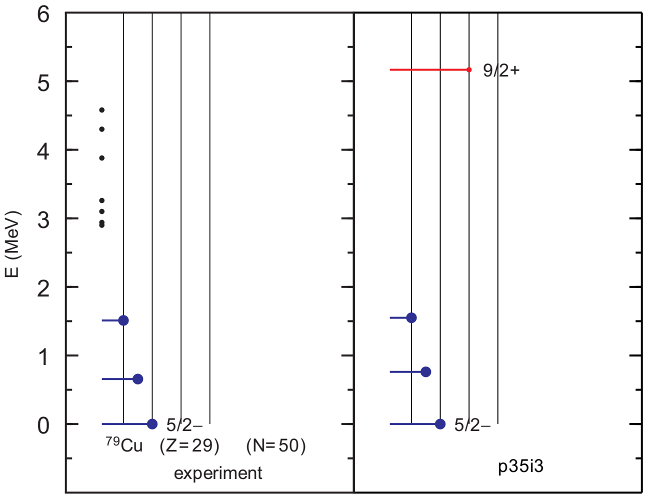

FIG. 7. Results for $^{79}$Cu.

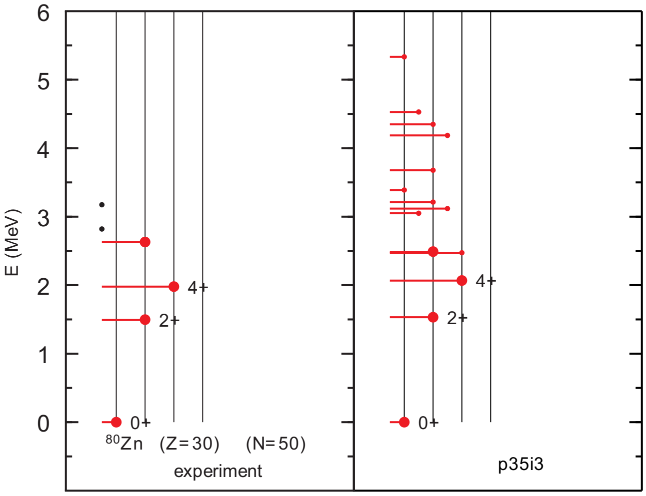

FIG. 8. Results for $^{80}$Zn.

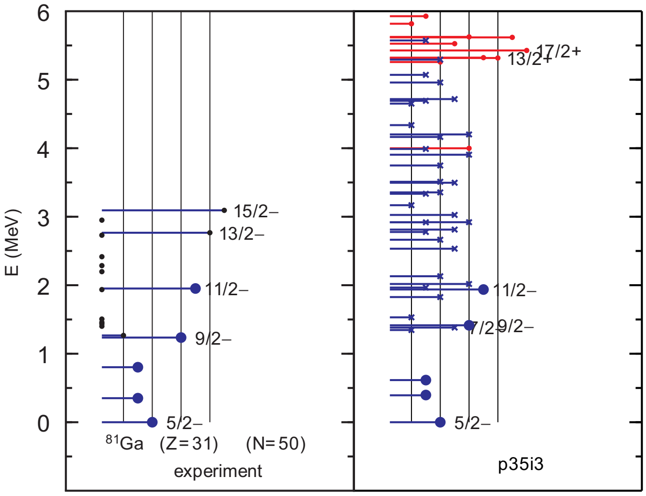

FIG. 9. Results for $^{81}$Ga.

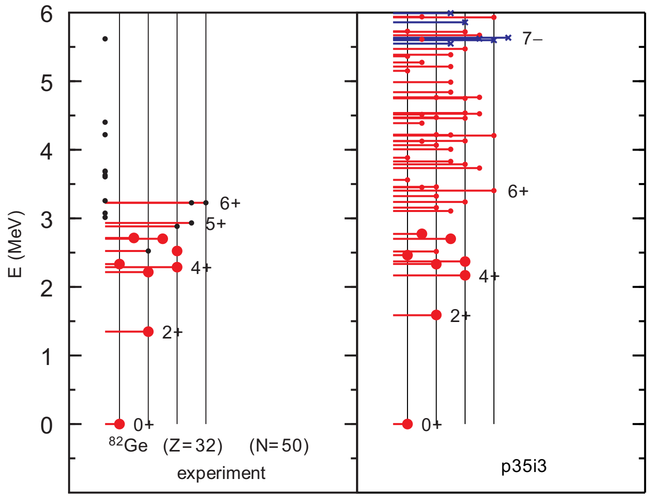

FIG. 10. Results for $^{82}$Ge.

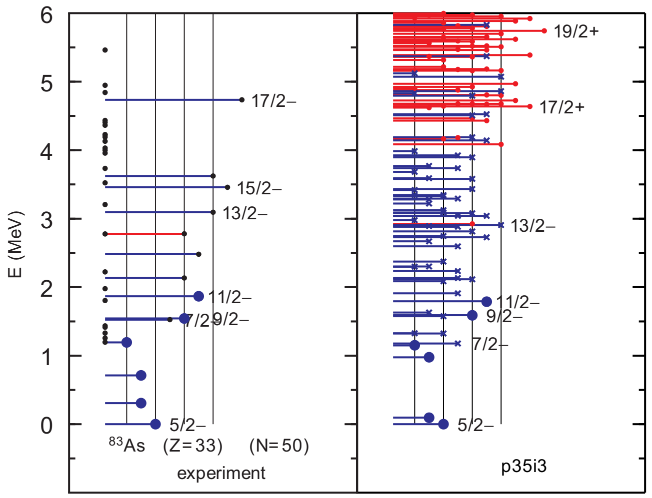

FIG. 11. Results for $^{83}$As.

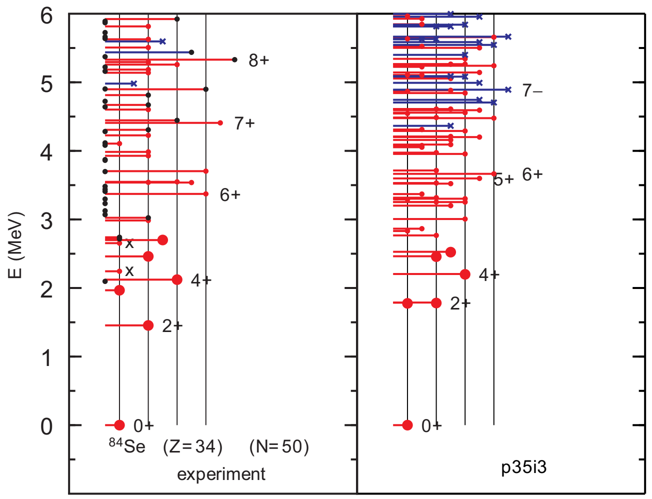

FIG. 12. Results for $^{84}$Se.

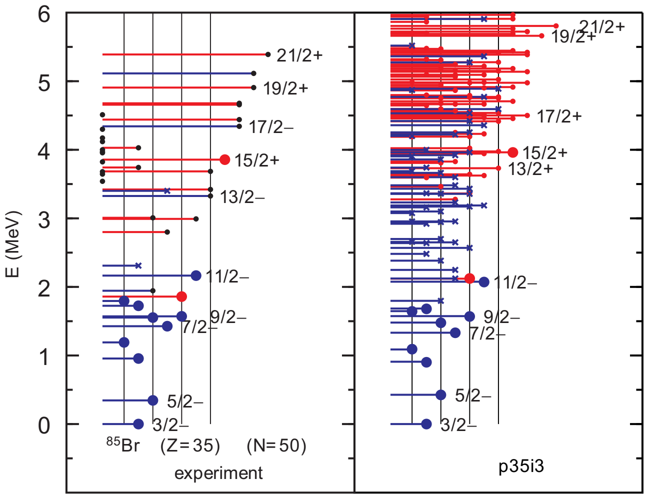

FIG. 13. Results for $^{85}$Br.

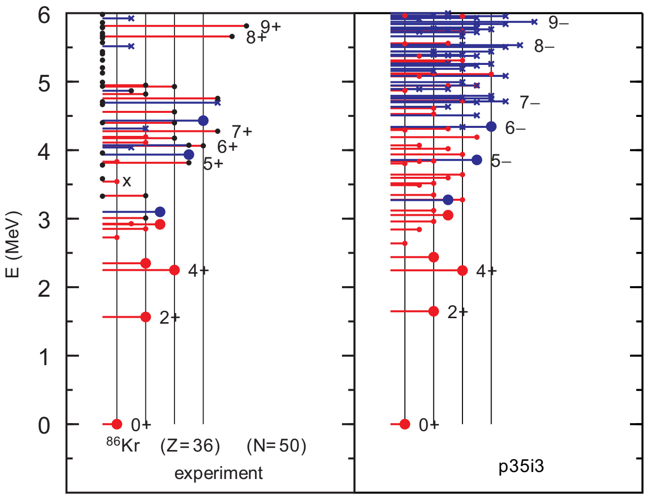

FIG. 14. Results for $^{86}$Kr.

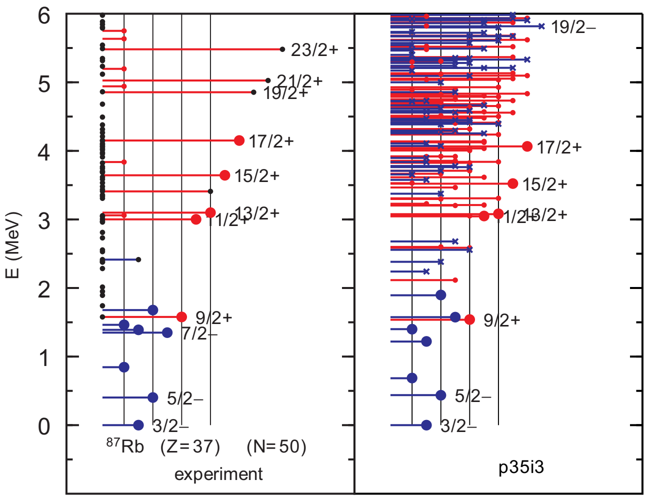

FIG. 15. Results for $^{87}$Rb.

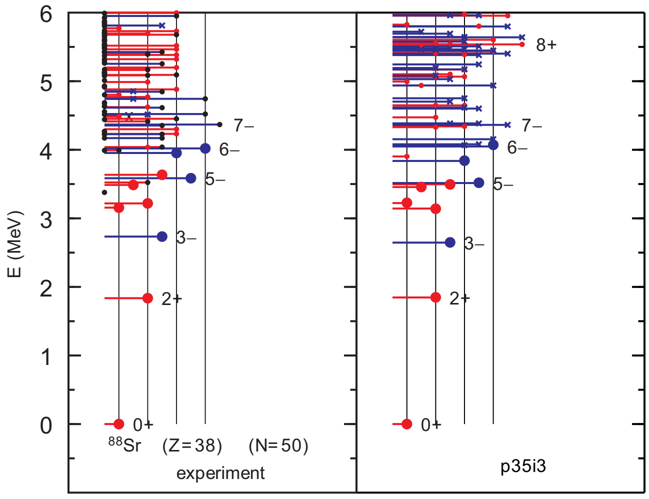

FIG. 16. Results for $^{88}$Sr.

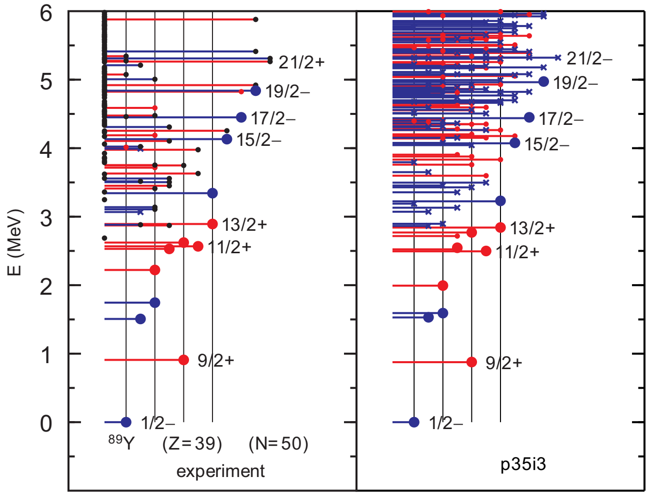

FIG. 17. Results for $^{89}$Y.

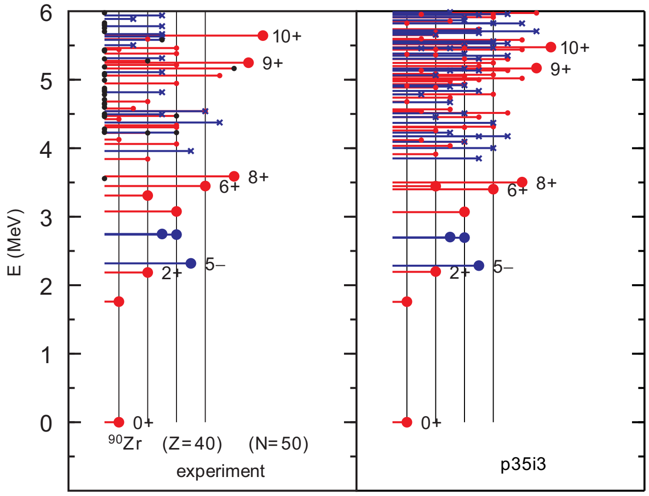

FIG. 18. Results for $^{90}$Zr.

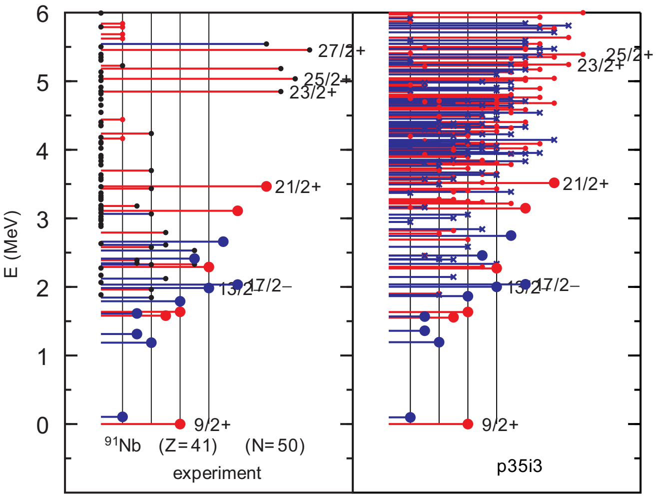

FIG. 19. Results for $^{91}$Nb.

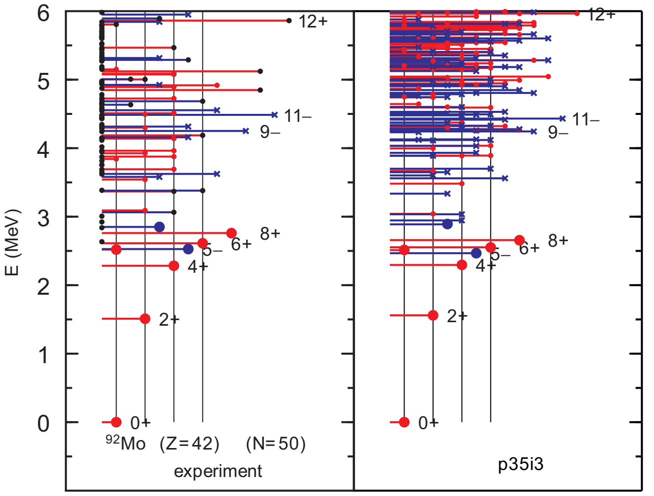

FIG. 20. Results for $^{92}$Mo.

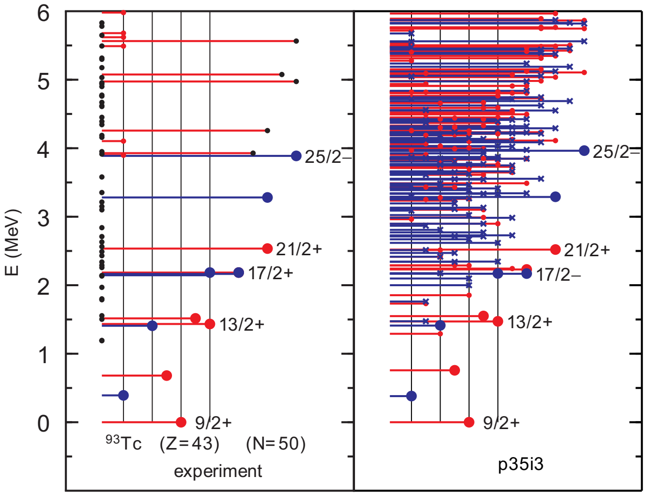

FIG. 21. Results for $^{93}$Tc.

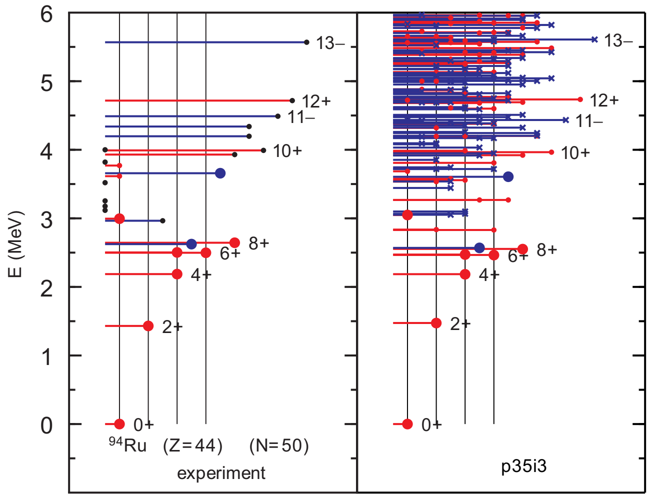

FIG. 22. Results for $^{94}$Ru.

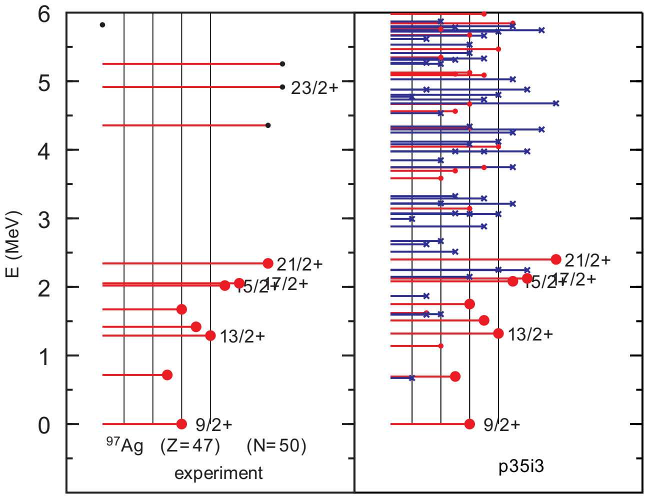

FIG. 25. Results for $^{97}$Ag.

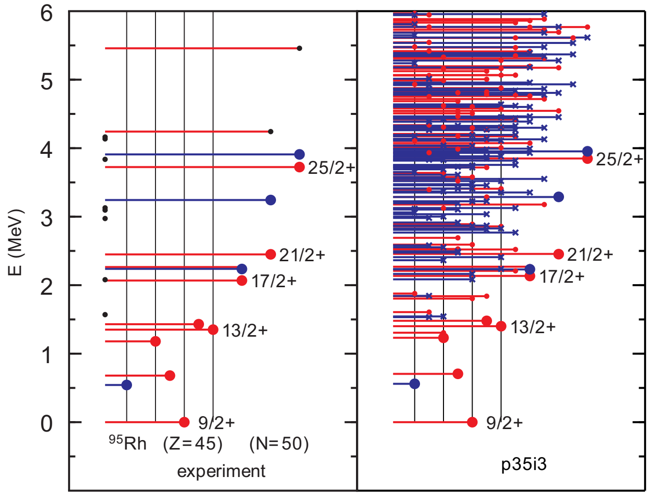

FIG. 23. Results for $^{95}$Rh.

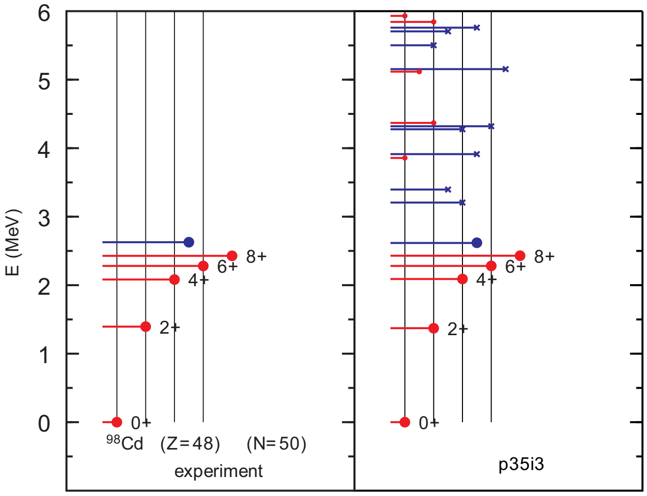

FIG. 26. Results for $^{98}$Cd.

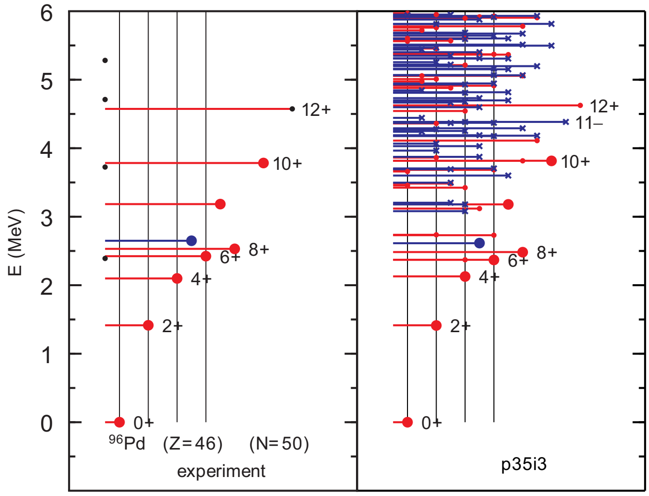

FIG. 24. Results for $^{96}$Pd.

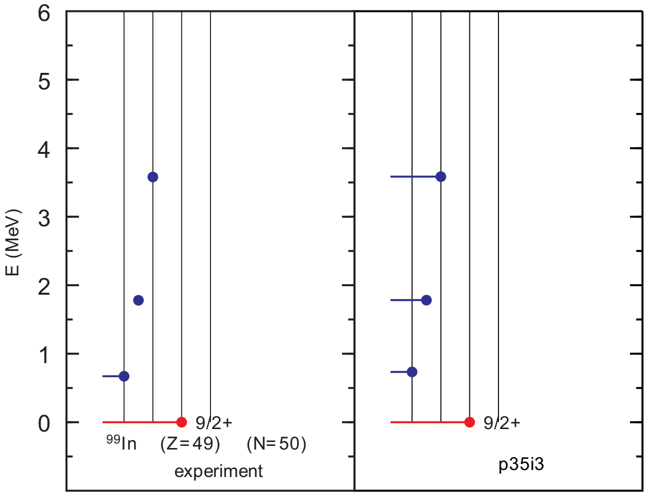

FIG. 27. Results for $^{99}$In.

of the state (red for odd, blue for even) and the length of the line gives the $J$ value of that state. States with only a black dot have an experimentally well-determined energy, but no definitely assigned $J^\pi$ value. States which have a colored bar but with only a black dot at the end have well-determined energy and parity, but have a tentatively assigned $J$ value. The large circles on the experimental levels on the left-hand side are those that were used for the SVD fits with results shown by the levels with large circles on the right-hand side. The black "X" marks in $^{84}$Se are $0^+$ intruder states coming from neutron two-particle two-hole excitations across the $N = 50$ neutron shell gap [54].

[1] B. A. Brown and W. A. Richter, Phys. Rev. C **74**, 034315 (2006).
[2] A. Magilligan and B. A. Brown, Phys. Rev. C **101**, 064312 (2020).
[3] B. C. He and S. R. Stroberg, Phys. Rev. C **110**, 044317 (2024).
[4] M. Hjorth-Jensen, T. T. S. Kuo, and E. Osnes, Phys. Rep. **261**, 125 (1995).
[5] Z. H. Sun, T. D. Morris, G. Hagen, G. R. Jansen, and T. Papenbrock, Phys. Rev. C **98**, 054320 (2018).
[6] S. R. Stroberg, H. Hergert, S. K. Bogner, and J. D. Holt, Annu. Rev. Nucl. Part. Sci. **69**, 307 (2019).
[7] M. Honma, T. Otsuka, B. A. Brown, and T. Mizusaki, Phys. Rev. C **69**, 034335 (2004).
[8] M. Honma, T. Otsuka, T. Mizusaki, and M. Hjorth-Jensen, Phys. Rev. C **80**, 064323 (2009).
[9] S. Mukhopadhyay, B. P. Crider, B. A. Brown, S. F. Ashley, A. Chakraborty, A. Kumar, M. T. McEllistrem, E. E. Peters, F. M. Prados-Estevez, and S. W. Yates, Phys. Rev. C **95**, 014327 (2017).
[10] A. Arima, S. Cohen, R. D. Lawson, and M. H. MacFarlane, Nucl. Phys. A **108**, 94 (1968).
[11] B. H. Wildenthal, Prog. Part. Nucl. Phys. **11**, 5 (1984).
[12] X. Ji and B. H. Wildenthal, Phys. Rev. C **37**, 1256 (1988).
[13] A. F. Lisetskiy, B. A. Brown, M. Horoi, and H. Grawe, Phys. Rev. C **70**, 044314 (2004).
[14] Q. Yuan and B. S. Hu, Phys. Lett. B **858**, 139018 (2024).
[15] I. Talmi and I. Unna, Nucl. Phys. **19**, 225 (1960).
[16] S. Cohen, R. D. Lawson, M. H. Macfarlane, and M. Soga, Phys. Lett. **10**, 195 (1964).
[17] N. Auerbach and I. Talmi, Nucl. Phys. **64**, 458 (1965).
[18] J. Vervier, Nucl. Phys. **75**, 17 (1966).
[19] J. B. Ball, J. B. McGrory, and J. S. Larsen, Phys. Lett. B **41**, 581 (1972).
[20] D. H. Gloeckner and F. J. D. Serduke, Nucl. Phys. A **220**, 477 (1974).
[21] J. Blomqvist and L. Rysdtrom, Phys. Scr. **31**, 31 (1985).
[22] L. Olivier *et al.*, Phys. Rev. Lett. **119**, 192501 (2017).
[23] L. Nies *et al.*, Phys. Rev. Lett. **131**, 022502 (2023).
[24] V. Vaquero *et al.*, Phys. Rev. Lett. **124**, 022501 (2020).
[25] K. Hebeler, S. K. Bogner, R. J. Furnstahl, A. Nogga, and A. Schwenk, Phys. Rev. C **83**, 031301(R) (2011).
[26] ENSDF database, http://www.nndc.bnl.gov/ensarchivals/.
[27] See Supplemental Material at http://link.aps.org/supplemental/10.1103/PhysRevC.111.044313 for the p35i3-svd-fit-results.txt file that contains a list of the experimental energy data used for the SVD fit together with the final theoretical energies obtained with the p35-i3 Hamiltonian, and the p35i3-tbme.txt file that contains a list of the SPE and TBME for the p35-i3 Hamitonian.
[28] R. Taniuchi *et al.*, Nature (London) **569**, 53 (2019).
[29] J. Taprogge *et al.*, Eur. Phys. J. A **52**, 347 (2016).
[30] J. Van de Walle *et al.*, Phys. Rev. Lett. **99**, 142501 (2007).
[31] Y. Shiga *et al.*, Phys. Rev. C **93**, 024320 (2016).
[32] Y. Tsunoda, T. Otsuka, N. Shimizu, M. Honma, and Y. Utsuno, Phys. Rev. C **89**, 031301(R) (2014).
[33] M. L. Cortes *et al.*, Phys. Rev. C **97**, 044315 (2018).
[34] V. Paziy *et al.*, Phys. Rev. C **102**, 014329 (2020).
[35] B. Cheal *et al.*, Phys. Rev. Lett. **104**, 252502 (2010).
[36] J. Dudouet *et al.*, Phys. Rev. C **100**, 011301(R) (2019).
[37] G. Maquart, Physique nucleaire experimental, thesis, Universtite de Lyon, 2017, https://theses.hal.science/tel-01684908v1.
[38] L. Olivier, Ph.D. thesis, University Paris-Saclay, 2017.
[39] M. F. Alshudifat *et al.*, Phys. Rev. C **93**, 044325 (2016).
[40] D. Verney *et al.*, Phys. Rev. C **76**, 054312 (2007).
[41] T. Rząca-Urban, W. Urban, J. L. Durell, A. G. Smith, and I. Ahmad, Phys. Rev. C **76**, 027302 (2007).
[42] J. K. Hwang, J. H. Hamilton, A. V. Ramayya, N. T. Brewer, Y. X. Luo, J. O. Rasmussen, and S. J. Zhu, Phys. Rev. C **84**, 024305 (2011).
[43] M. P. Carpenter *et al.*, Physics Division Annual Report 2006, Argonne National Laboratory, https://www.phy.anl.gov/division/publications/annual_report/2006/Part%20I%20Annual%20Report%202006.pdf.
[44] E. Sahin, G. de Angelis, G. Duchene, T. Faul, A. Gadeaa, A. F. Lisetskiy, D. Ackermann, A. Algora, S. Aydinhi, F. Azaiez *et al.*, Nucl. Phys. A **893**, 1 (2012).
[45] D. Wilmsen, thesis, Universite de Caen Normandie, 2017.
[46] D. Thisse *et al.*, Eur. Phys. J. A **59**, 153 (2023).
[47] K. Sieja and F. Nowacki, Phys. Rev. C **85**, 051301(R) (2012).
[48] A. Gade *et al.*, Phys. Rev. C **81**, 064326 (2010).
[49] P. Bączyk, W. Urban, D. Zlotowska, M. Czerwinski, T. Rzaca-Urban, A. Blanc, M. Jentschel, P. Mutti, U. Koster, T. Soldner, G. de France, G. Simpson, and C. A. Ur, Phys. Rev. C **91**, 047302 (2015).
[50] K. Rezynkina *et al.*, Phys. Rev. C **106**, 014320 (2022).
[51] F. Drouet, G. S. Simpson, A. Vancraeyenest, G. Gey, G. Kessedjian, T. Malkiewicz, M. Ramdhane, C. Sage, G. Thiamova, T. Grahn *et al.*, EPJ Web Conf. **62**, 01005 (2013).
[52] M. G. Porquet *et al.*, Phys. Rev. C **84**, 054305 (2011).
[53] J. A. Winger, J. C. Hill, F. K. Wohn, R. L. Gill, X. Ji, and B. H. Wildenthal, Phys. Rev. C **38**, 285 (1988).
[54] S. M. Mullins, D. L. Watson, and H. T. Fortune, Phys. Rev. C **37**, 587 (1988).
[55] P. Hoff and B. Fogelberg, Nucl. Phys. A **368**, 210 (1981).
[56] J. Litzinger *et al.*, Phys. Rev. C **92**, 064322 (2015).
[57] J. D. Knight, C. J. Orth, W. T. Leland, and A. B. Tucker, Phys. Rev. C **9**, 1467 (1974).
[58] W. Urban *et al.*, Phys. Rev. C **94**, 044328 (2016).
[59] A. Prevost *et al.*, Eur. Phys. J. A **22**, 391 (2004).
[60] G. Winter, L. Funke, R. Schwengner, H. Prade, R. Wirowski, N. Nicolay, A. Dewald, and P. von Brentano, Z. Phys. A **343**, 369 (1992).
[61] M. Wang *et al.*, Chin. Phys. C **45**, 030003 (2021).
[62] M. Mougeot *et al.*, Nat. Phys. **17**, 1099 (2021).
[63] C. B. Hinke *et al.*, Nature (London) **486**, 341 (2012).